ADVANCED SCIENCE Open Access
www.advancedscience.com

Electric-Field Manipulation of Magnetic Chirality in a Homo-Ferro-Rotational Helimagnet

Junjie Yang, Masaaki Matsuda, Trevor Tyson, Joshua Young, William Ratcliff, Yunpeng Gao, Dimuthu Obeysekera, Xiaoyu Guo, Rachel Owen, Liuyan Zhao, and Sang-wook Cheong*

Ferro-rotational (FR) materials, renowned for their distinctive material functionalities, present challenges in the growth of homo-FR crystals (i.e., single FR domain). This study explores a cost-effective approach to growing homo-FR helimagnetic $RbFe(SO_4)_2$ (RFSO) crystals by lowering the crystal growth temperature below the T_{FR} threshold using the high-pressure hydrothermal method. Through polarized neutron diffraction experiments, it is observed that nearly 86% of RFSO crystals consist of a homo-FR domain. Notably, RFSO displays remarkable stability in the FR phase, with an exceptionally high T_{FR} of ≈573 K. Furthermore, RFSO exhibits a chiral helical magnetic structure with switchable ferroelectric polarization below 4 K. Importantly, external electric fields can induce a single magnetic domain state and manipulate its magnetic chirality. The findings suggest that the search for new FR magnets with outstanding material properties should consider magnetic sulfates as promising candidates.

1. Introduction

Ferro-rotational (FR) materials that exhibit spontaneous ordering of crystallographic rotational distortions have garnered significant attention due to their unique material functionalities.[1–12] These rotational distortions can arise from either clockwise (CW) or counterclockwise (CCW) rotations of atomic polyhedra within crystals, leading to the emergence of an axial-vector order parameter known as Ferro-rotation (FR) across extensive spatial dimensions.[5,13] When combined with the non-collinear helical spin order, this FR order can result in multiferroicity in FR helimagnets.[2,12] Remarkably, multiferroicity in FR helimagnets opens up the potential to manipulate various material properties using electric fields. This includes controlling the helical spin order and spin waves, paving the way for innovative device designs.[14–18] However, achieving the manipulation of material properties under electric fields in FR helimagnets necessitates the presence of a homo-FR domain state (i.e., a single FR domain which is either CCW or CW). In contrast to other ferroic materials, like ferroelectric materials, where the ferroelectric domain can be easily controlled by the conjugate electric field $\vec{E}$, the conjugate field to FR order is the curl of $\vec{E}$, i.e., $\nabla \times \vec{E}$, which often lacks the required intensity to govern the FR domain.[13] Consequently, growing homo-FR helimagnets presents significant challenges, and there is limited literature documenting successful attempts with known FR helimagnets.

J. Yang, T. Tyson, Y. Gao, D. Obeysekera
Department of Physics
New Jersey Institute of Technology
Newark, NJ 07102, USA
E-mail: jyang@njit.edu
J. Yang, M. Matsuda
Neutron Scattering Division
Oak Ridge National Laboratory
Oak Ridge, TN 37831, USA
J. Young
Department of Chemical and Materials Engineering
New Jersey Institute of Technology
Newark, NJ 07102, USA
W. Ratcliff
NIST Center for Neutron Research
National Institute of Standards and Technology
Gaithersburg, MD 20899, USA
W. Ratcliff
Department of Materials Science and Engineering
Department of Physics
University of Maryland
College Park, MD 20741, USA
X. Guo, R. Owen, L. Zhao
Department of Physics
University of Michigan
Ann Arbor, MI 48109, USA
S.-wook Cheong
Rutger Center for Emergent Materials and Department of Physics and Astronomy
Rutgers University
Piscataway, NJ 08854, USA

The ORCID identification number(s) for the author(s) of this article can be found under https://doi.org/10.1002/advs.202402048

© 2024 The Author(s). Advanced Science published by Wiley-VCH GmbH. This is an open access article under the terms of the Creative Commons Attribution License, which permits use, distribution and reproduction in any medium, provided the original work is properly cited.

DOI: 10.1002/advs.202402048

The search for new FR helimagnets that require the growth of a homo-FR domain is crucial for exploring the functionalities of FR materials. One approach is to seek out materials with a high FR transition temperature (T_{FR}) and a low crystal growth temperature (T_g), especially when $T_g < T_{FR}$. In such cases, the crystal may naturally develop into a homo-FR domain during the crystallization process. To date, known FR magnets either have $T_g > T_{FR}$, as seen in $RbFe(MoO_4)_2$ (RFMO) and $CaMn_7O_{12}$ (CMO), resulting in a multi-domain state, or they exhibit collinear spin order rather than the desired non-collinear helical order, as observed in $MTiO_3$ (M = Mn, Fe, and Ni).[1,2,5,19,20] Sulfate-containing magnetic ions may serve as promising candidates for achieving high T_{FR} with magnetic order. Compared to other oxygen polyhedra, SO_4 ions are smaller, thus possessing higher mobility features that can manifest strong rotational properties. However, very few magnetic sulfates have been reported to form bulk single crystals, primarily due to growth challenges. This limitation hinders the revelation of their exotic material functionalities. For instance, the magnetic anhydrous sulfate $AM(SO_4)_2$ (where A = K, Rb, Cs, and M = Cr or Fe) exhibits potential FR $P\bar{3}$ space group at room temperature, with magnetic ordering occurring below 4 K, as suggested by previous powder diffraction results.[21–24] However, to date, only powder samples have been available, with none successfully grown into single crystals. Consequently, the precise nature of these materials remains poorly understood.

In our current research, we have successfully obtained unique homo-FR helimagnetic crystals of magnetic anhydrous sulfate $RbFe(SO_4)_2$ (RFSO) using a cost-effective hydrothermal method. Our X-ray diffraction analysis confirms that RFSO possesses an exceptionally high T_{FR} of ≈573 K, significantly exceeding its T_g of ≈483 K. Our first-principle calculations indicate that the high T_{FR} in RFSO is a result of the extremely high stability of the SO_4 tetrahedra in the FR phase. Additionally, polarized neutron diffraction studies reveal that roughly 86% of the RFSO crystal consists of a homo-FR domain. At temperatures below 4.0 K, RFSO exhibits a chiral helical spin order and a ferroelectric polarization along the *c*-axis. An external electric field can induce a single magnetic chiral domain state and manipulate the magnetic chirality within the single domain. The availability of homo-FR RFSO crystals with exceptional tunability of magnetic chirality by electric field opens up exciting possibilities for future device configurations, such as electric-field tunable spin-wave diodes. This study suggests the potential for synthesizing new homo-FR helimagnets with unique properties and applications within SO_4-based magnetic materials.

2. Results and Discussion

Under the condition of $T_g < T_{FR}$, a tiny nucleus forms at the initial stage of crystal growth, likely a homo-FR domain due to its small size. As the crystallization progresses, this homo-FR domain nucleus acts as a seed, absorbing free atoms and propagating its homo-FR structure outward to form a bulk crystal. Conversely, when $T_g > T_{FR}$, as exemplified by RFMO with $T_{FR} \approx 190$ K and $T_g > 700$ K and CMO with $T_{FR} \approx 440$ K and $T_g \approx 923$ K, once the crystal cools below T_{FR}, both CW and CCW domains populate equally.[2,25,26] This scenario emphasizes the importance of identifying an FR system with a high T_{FR} and utilizing a growth method capable of significantly reducing T_g. Hence, we chose RFSO for our study, where the SO_4 polyhedra may have greater stability than MoO_4 in the FR phase, and thus have high T_{FR}. For crystal growth, we opted for the low-cost hydrothermal method, which provides a high-pressure environment, enhancing the solubility of RFSO in the solvent and thereby reducing T_g. Our RFSO crystals were successfully grown at 483 K, exhibiting a hexagonal platelike morphology, as depicted in the inset of **Figure 1A**. Detailed growth information can be found in the experimental section. To determine the precise crystal structure of RFSO, we conducted synchrotron X-ray diffraction experiments on an RFSO crystal (#1). Figure 1A,B show the X-ray diffraction patterns obtained at room temperature. Bright spots at the intersection of the (*h*, *k*, *l*) grids are the Bragg reflections of RFSO single crystal. The broad dark stripes are from dead zones in the area detector, separating active regions, and the sun-like disks at the center are due to air scattering as well as scattering from epoxy holding the crystal to the support fiber. The crystal structure was refined in three different space groups: $P\bar{3}$, *P*321, and $P\bar{3}m1$, with results summarized in **Table 1**. The methods used to analyze the single-crystal X-ray diffraction data and the refined parameters of the $P\bar{3}$, *P*321, and $P\bar{3}m1$ models are presented in the Supporting Information. Among these space groups, $P\bar{3}$ was determined to offer the best fit to the data (smallest R_1, smallest residual, and *GOF* close to 1.0), corresponding to the FR structure. The $P\bar{3}$ structure is depicted in Figure 1C,D, and it is composed of alternating layers of SO_4 tetrahedra, FeO_6 octahedra, and Rb ions. As shown in Figure 1C,D, the SO_4 tetrahedra exhibit a CCW rotation around the *c*-axis for the type-I FR domain, while for the type-II FR domain, they display a CW rotation (as shown in Figure S2A,B, Supporting Information). The angle γ, representing the rotation of SO_4 relative to the *a*-axis, is ≈25°.

To determine the T_{FR} of RFSO, high-temperature synchrotron powder X-ray diffraction measurements were conducted on an RFSO powder sample (crushed crystals). Figure 1E shows the contour plot of diffraction patterns ranging from 323 to 823 K. A continuous transition is observed near 573 K, indicated by the merging of (202) and (104) peaks of the $P\bar{3}$ structure, suggesting a $T_{FR} \approx 573$ K which is significantly higher than that of RFMO ($T_{FR} \approx 190$ K). To gain a better understanding of the high T_{FR} in RFSO, we conducted Density Functional Theory (DFT) calculations, comparing it with its counterpart RFMO. First, we fully optimized the crystal structures of both RFSO and RFMO in both the FR $P\bar{3}$ and non-FR $P\bar{3}m1$ phases (see Figure S2C–F, Supporting Information). Subsequently, we calculated the energy as

Table 1. Quality of Fit Parameters for Different Space Groups. The R_1 is defined as $R_1 = \sum||F_o| - |F_c||/\sum|F_o|$, where F_o is the measured scattering amplitude and F_c is the calculated amplitude. The residual (charge) represents the Max and Min Peak in the Final Difference Map. The *GOF* (Goodness of fit) is defined as $GOF = \{\sum w(F_2^O - F_2^c)^2/(n-p)\}^{1/2}$, where w is the weight, n is the number of reflections, and p is the total number of fitting parameters.

Space Group[a)]	R_1	Residual [e A^{-3}]	*GOF*	Temperature [K]
$P\bar{3}$	3.90%	2.12/−1.26	1.076	290
*P*321	8.65%	3.29/−2.06	1.164	290
$P\bar{3}m1$	11.50%	4.93/−2.06	1.266	290

[a)] Refined Rb occupancy is 0.870(4) for $P\bar{3}$, 0.849(15) for *P*321, 1.02(2) for $P\bar{3}m1$.

© 2024 The Author(s). Advanced Science published by Wiley-VCH GmbH

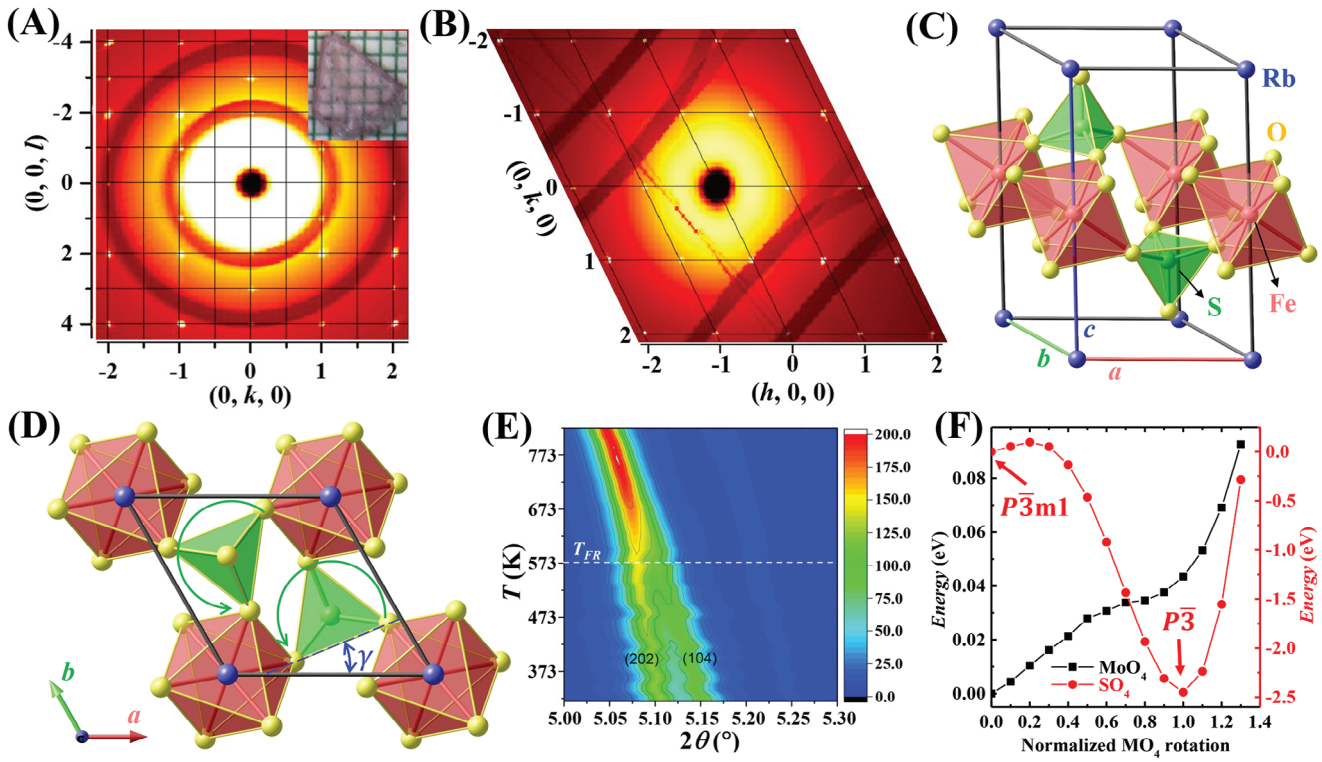

Figure 1. A) X-ray single crystal diffraction pattern in the (0, *k*, *l*) plane at 290 K. The inset displays a photograph of an RFSO single crystal on a millimeter-grid paper. B) X-ray single crystal diffraction pattern in the (*h*, *k*, 0) plane at 290 K. C) Refined crystal structure of RFSO at 290 K. D) The CCW rotational distortions (green circles with arrows) of SO_4 and FeO_6 for the type-I FR domain. The angle γ represents the rotational distortion relative to the *a*-axis. These rotational distortions break mirror reflection symmetries in the *ab* plane. E) Temperature-dependent X-ray diffraction patterns for an RFSO powder sample. The white dashed line serves as a guide to visualize the FR phase transition. F) Calculated energy as a function of MO_4 (M = S or Mo) polyhedral rotation angle for RFSO (red curve) and RFMO (black curve). The rotation angle is normalized to the equilibrium rotational angle identified in the optimized $P\bar{3}$ structure.

a function of the rotational angle of MO_4 (M = S or Mo), as illustrated in Figure 1F. In Figure 1F, the rotational angles are normalized to that of the optimized $P\bar{3}$ phase for each material. In the case of RFSO, the energy-rotation curve displays a deep valley near the optimized $P\bar{3}$ phase (i.e., where the normalized SO_4 rotation equals to 1), with an energy gain of 2.5 eV induced by the SO_4 rotation. A slight deviation from the optimized $P\bar{3}$ phase significantly decreases the energy gain. In contrast, the energy-rotation curve of RFMO is nearly flat, and MoO_4 rotation does not result in a significant energy gain. These results suggest that the rotational distortion of SO_4 in RFSO is highly stable, and the high T_{FR} observed in RFSO is attributed to the stability of SO_4 rotation, which is significantly more energetically unfavorable to turn off (leading to the non-FR $P\bar{3}m1$ phase) compared to MoO_4 rotations.

The RFSO crystals grown under the condition of $T_g < T_{FR}$ is likely homo-FR. However, determining the population of FR domains within a bulk crystal presents challenges. Thanks to the interactions between FR and magnetic order, an alternative approach to utilizing magnetic peaks by the neutron diffraction method is feasible. Unpolarized neutron diffraction experiments were conducted on an RFSO crystal (#2, ≈5 × 5 × 1 mm^3). **Figure** 2A displays the neutron diffraction patterns in the (*h*, *h*, *l*) plane at 1.6 K. A pair of incommensurate magnetic peaks were observed at (1/3, 1/3, 0.5 ± Δ) with Δ ≈0.07. Our representational analysis, outlined in detail in the Supporting Information, of the magnetic peaks indicates the possibility of three magnetic structures: Γ_1, Γ_2, and Γ_3.[27–30] Γ_1 corresponds to a spin-density wave structure (see Figure S3A, Supporting Information) with magnetic moments aligned along the *c*-axis, which is non-chiral. On the other hand, Γ_2 and Γ_3 represent left-handed and right-handed chiral helical magnetic structures (see Figure S3B,C, Supporting Information), respectively. As discussed later in this manuscript, our polarized neutron diffraction results revealed the magnetic chirality in RFSO, decisively excluding the possibility of the Γ_1 structure. Either Γ_2 or Γ_3 yields a chiral magnetic structure with a 120° configuration within each layer and a chiral helical twist between adjacent layers along the *c*-axis. Figure 2C–F shows the chiral helical magnetic structure of RFSO at 1.6 K. It's worth noting that another pair of incommensurate magnetic peaks were also observed at (2/3, 2/3, 0.5 ± Δ) (Figure S4A, Supporting Information). Figure 2B displays the temperature dependence of the (1/3, 1/3, 0.5 ± Δ) peaks, with peak intensities increasing below 4 K, suggesting a magnetic ordering temperature of 4 K. This is consistent with the results of the temperature-dependent magnetic moment (*M*–*T*) shown in the inset of Figure 2B. The *M*–*T* curve exhibits a distinct peak at 4 K, indicating an antiferromagnetic transition at $T_N \approx 4$ K.

The chiral helical magnetic structure in RFSO may arise from its FR order. The FR order breaks mirror reflection symmetries

© 2024 The Author(s). Advanced Science published by Wiley-VCH GmbH

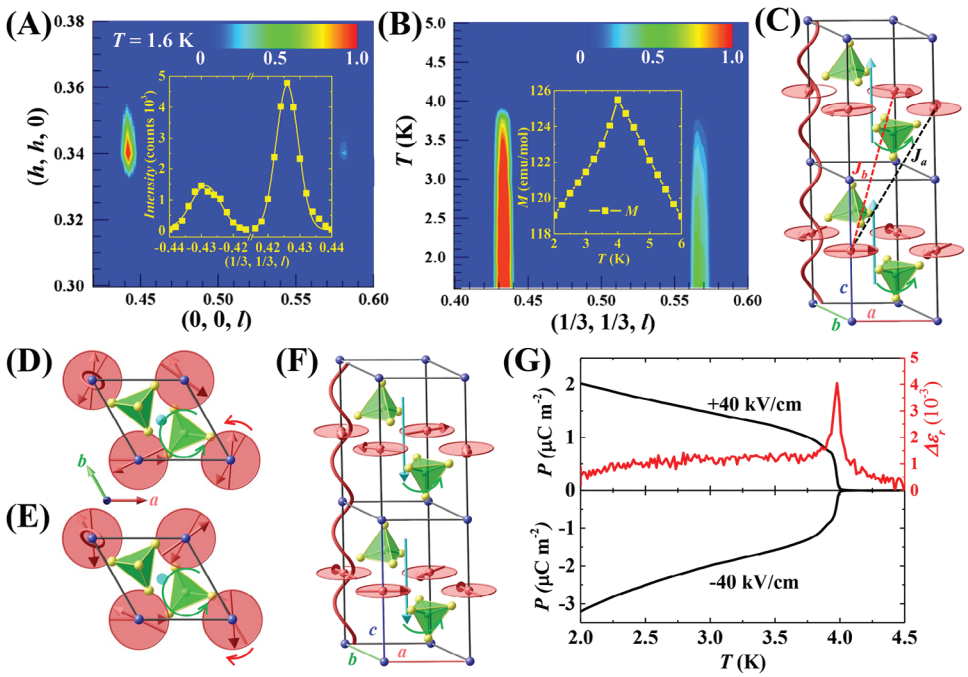

Figure 2. A) Unpolarized neutron diffraction pattern in the (*h*, *h*, *l*) scattering plane measured at 1.6 K on RFSO single crystal (#2). The inset provides a comparison of neutron diffraction intensity at (1/3, 1/3, –0.43) and (1/3, 1/3, +0.43) magnetic peaks. Error bars in this paper represent one standard deviation. B) Temperature dependence of the (1/3, 1/3, 0.43) and (1/3, 1/3, 0.57) magnetic peaks. The inset displays the temperature dependence of the magnetic moment for an RFSO single crystal when a magnetic field is applied to the *ab* plane with a magnitude of 0.2 T. C,D) A CCW FR domain with a right-handed helical magnetic structure exhibits upward electric polarization (light blue arrow). The green circle arrow in represents the FR order, and the red circle arrow in illustrates the twist of magnetic moments in the adjacent layers. The black dashed line in (C) indicates the super-exchange path J_a, while the red dashed line illustrates J_b. E,F) A CCW FR domain with a left-handed helical magnetic structure exhibits downward electric polarization (light blue arrow). G) Electric polarization P_c as a function of temperature (black left axis). The right red axis exhibits the relative change of dielectric constant as a function of temperature, represented as $\Delta\epsilon = \epsilon(T)\text{-}\epsilon(5\ \mathrm{K})$.

in the *ab* plane of RFSO, resulting in nonequivalent super-super-exchange terms J_a (dashed black) and J_b (dashed red) bridging adjacent triangular lattice layers, as illustrated in Figure 2C. These nonequivalent J_a and J_b terms induce a relative twist between adjacent layers, leading to the chiral helical magnetic structure. The two distinct FR domains have different values of J_a and J_a: if J_a is smaller than J_a in the CW domain, then it should be the case that J_a is larger than J_b in the CCW domain.[1] Consequently, the two FR domains exhibit distinct magnetic propagation vectors, denoted as $\vec{q}_1 = (\pm 1/3, \pm 1/3, \pm q_z)$ for CW domain, and $\vec{q}_2 = (\mp 1/3, \mp 1/3, \pm q_z)$ for the CCW domain.[1] In a crystal with an even distribution of FR domains, the magnetic peaks associated with $\vec{q}_1$ should exhibit comparable intensity to those of $\vec{q}_2$. However, as Figure 2A illustrates, the intensity of (1/3, 1/3, 0.43) significantly exceeds that of (1/3, 1/3, 0.57), indicating the dominance of one FR domain. This observation holds true for (2/3, 2/3, 0.5 ± Δ) (see Figure S4A, Supporting Information). As shown in the inset of Figure 2A, a fitting analysis on the (1/3, 1/3, 0.43) and (1/3, 1/3, −0.43) peaks reveals an integrated peak area ratio of 3.3:1, suggesting that the dominant FR domain constitutes ≈77% of the crystal. To further confirm the homo-FR state, we conducted Rotational-Anisotropy Second Harmonic Generation measurements at four positions on two different crystals (#3 and #4), indicating a homo-FR domain in RFSO crystals extending at least 2 mm (see Figure S5, Supporting Information), ≈50 times larger than that of RFMO (≈40 μm).[5]

To uncover the potential novel material functionalities in the (almost) homo-FR RFSO crystals, we have harnessed the concept of permutable Symmetry Operational Similarity (SOS) which has proven highly effective in comprehending material properties.[13,31–34] One key permutable SOS relationship is expressed as **A•C = P**.[34] Here, **A** represents the FR vector, **C** is chirality, and **P** corresponds to electric polarization. This relationship informs us that when an FR object **A** interacts with chirality **C**, the resultant **A•C** response manifests as an electric polarization **P**. The chiral helical magnetic structure observed in RFSO exhibits characteristics reminiscent of chirality **C**. Consequently, RFSO possesses ferroelectricity, and the direction of its ferroelectric polarization depends on the sense of FR and the chiral helical magnetic structure. We assume that the dominant FR domain in RFSO is of the CCW type. As visually depicted in Figure 2C–F, within a CCW FR system, a right-handed (left-handed) chiral helical magnetic structure induces an upward (downward) electric polarization along the *c*-axis. Conversely, within a CW FR system, a left-handed (right-handed) chiral helical magnetic structure results in an upward (downward) electric polarization. Furthermore, it's important to note that the SOS relationship **A•C = P** is permutable, meaning that **A•P = C** is also valid. This implies that the chirality of the helical magnetic structure can be controlled by the electric polarization. As illustrated in Figure 2C–F,

© 2024 The Author(s). Advanced Science published by Wiley-VCH GmbH

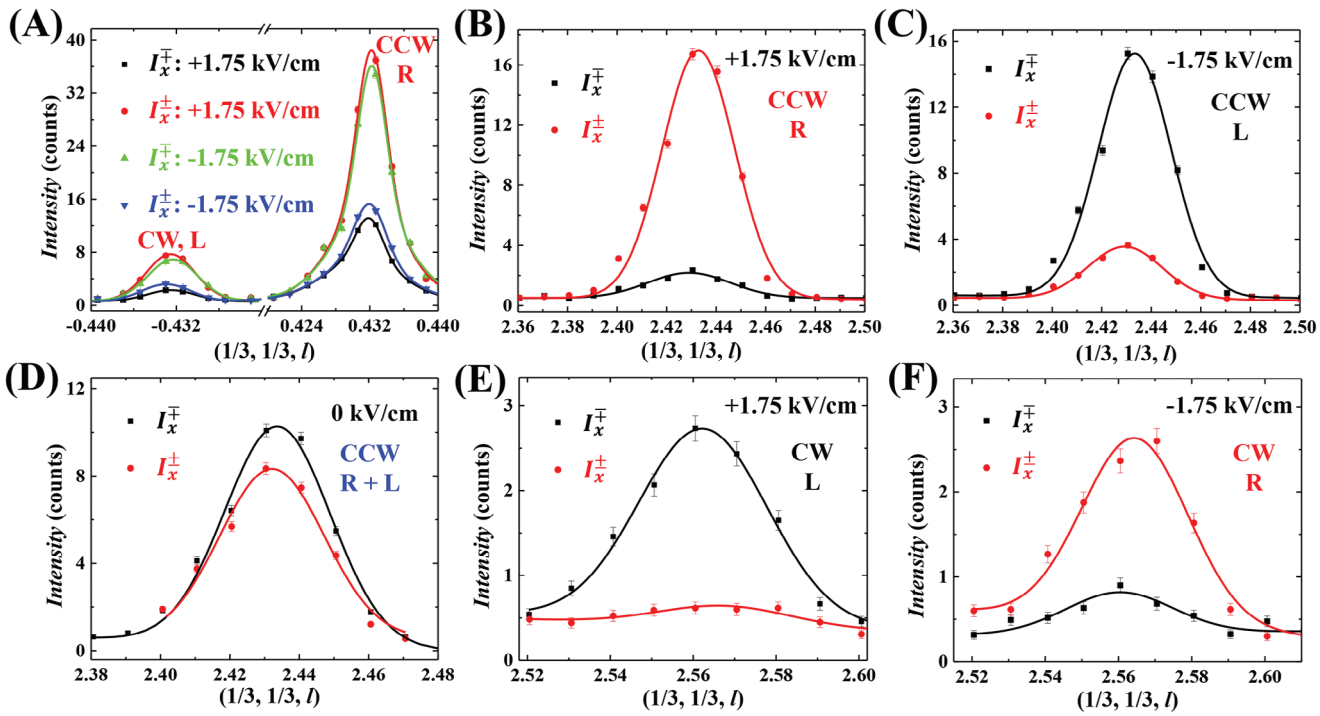

Figure 3. A) Intensities of $I_x^{\pm}$ and $I_x^{\mp}$ measured at (1/3, 1/3, –0.43) and (1/3, 1/3, 0.43) magnetic peaks with two different electric poling fields. B) Intensities of $I_x^{\pm}$ and $I_x^{\mp}$ measured at (1/3, 1/3, 2.43) with a +1.75 kV cm^{-1} poling field. C) Intensities of $I_x^{\pm}$ and $I_x^{\mp}$ measured at (1/3, 1/3, 2.43) with a –1.75 kV cm^{-1} poling field. D) Intensities of $I_x^{\pm}$ and $I_x^{\mp}$ measured at (1/3, 1/3, 2.43) with 0 kV cm^{-1} poling field. E) Intensities of $I_x^{\pm}$ and $I_x^{\mp}$ measured at (1/3, 1/3, 2.56) with +1.75 kV cm^{-1} poling field. F) Intensities of $I_x^{\pm}$ and $I_x^{\mp}$ measured at (1/3, 1/3, 2.56) with a –1.75 kV cm^{-1} poling field. All results were measured at 1.6 K. The CCW and CW letters indicate the type of FR domain, and the R and L letters signify the handedness of the magnetic domain.

inverting the polarization direction could switch the magnetic chirality in a homo-FR crystal.

We measured the electric polarization along the *c*-axis (P_c) of an RFSO crystal (#5) as a function of temperature (P_c–T). Before the measurement, the crystal was poled by an external electric field during the cooling process. Figure 2G exhibits the P_c–T curve obtained under a positive poling field +40 kV cm^{-1}. In line with the onset of helical magnetic order, P_c begins to increase at 4 K and reaches a value of ≈2.0 μC m^{-2} at 2 K. These observations provide strong evidence supporting the idea that the combination of FR and chiral helical magnetic structures can induce ferroelectric polarization. The temperature dependence of the dielectric constant ϵ was also measured. Figure 2G (on its right axis, shown in red) exhibits the relative change of dielectric constant as a function of temperature, represented as $\Delta\epsilon = \epsilon(T)$-$\epsilon$(5 K). A notable peak is observed at T_N ≈4 K in the $\Delta\epsilon$–T curve. To examine the switchability of P_c, the P_c–T curve was also measured under a negative poling field of −40 kV cm^{-1}. As shown in the bottom panel of Figure 2G, the polarization P_c is symmetric and switchable.

To ascertain whether the chirality of helical magnetic structure can be switched by an electric field, we performed the polarized neutron diffraction experiments on an RFSO crystal (#6, ≈3 × 3 × 1 mm^3). We define the *x*-axis along the direction of the scattering vector $\vec{Q}$, with *z* being vertical and *y* perpendicular to *x* in the scattering plane. The incident neutrons were polarized along the *x*-axis (i.e., $\vec{P}_i \parallel \vec{Q}$) and the analysis was performed in the same direction. With two possible polarization states for both incident and scattered neutrons (either parallel or antiparallel to *x*), we can measure four distinct intensities: I_x^{++}, I_x^{--}, $I_x^{\pm}$, and $I_x^{\mp}$. The $I_x^{\pm} \propto |M_\perp|^2 + P_i M_C$ and $I_x^{\mp} \propto |M_\perp|^2 - P_i M_C$, where $M_\perp$ is the magnetic component perpendicular to $\vec{Q}$ and M_C is the magnetic chiral term with $M_C = i(M_\perp^{y*} M_\perp^z - M_\perp^{z*} M_\perp^y)$. For an effective comparison of the measured magnetic chirality at different magnetic peaks, we introduce a normalized magnetic chirality $m_C = (I_x^{\pm} - I_x^{\mp})/(I_x^{\pm} + I_x^{\mp})$. The crystal was initially poled under +1.75 kV cm^{-1} upon cooling. Given the poling process, each FR domain would coincide with a single ferroelectric domain and a single magnetic helical domain. To deduce the proportion of the two FR domains, we compared the intensity of $I_x^{\pm}$ (or $I_x^{\mp}$) for the two (1/3, 1/3, ± 0.43) peaks, corresponding to the two distinct FR domains. Integrated intensities of these peaks were computed from their fittings, as shown in **Figure** 3A. For +1.75 kV cm^{-1} (red curves), the integrated intensities of $I_x^{\pm}$ at (1/3, 1/3, 0.43) is ≈6.2 times larger than that of (1/3, 1/3, –0.43), suggesting a ratio of 86% for the dominant FR domain in crystal #6. These results indicate crystal #6 is largely a homo-FR crystal, with the dominant FR domain assumed to be CCW. Moreover, the prominence of $I_x^{\pm}$ over $I_x^{\mp}$ at (1/3, 1/3, 0.43) suggests a right-handed magnetic chirality in the dominant CCW FR domain for +1.75 kV cm^{-1}, with an estimated m_C of +0.46 based on the integrated intensities. For (1/3, 1/3, –0.43) peak, the $I_x^{\pm}$ is also stronger than $I_x^{\mp}$. However, since the scattering vector q_z is negative, the magnetic domain associated with the minor CW FR domain is left-handed, leading to a negative m_C ≈ –0.62. When the crystal is poled under

© 2024 The Author(s). Advanced Science published by Wiley-VCH GmbH

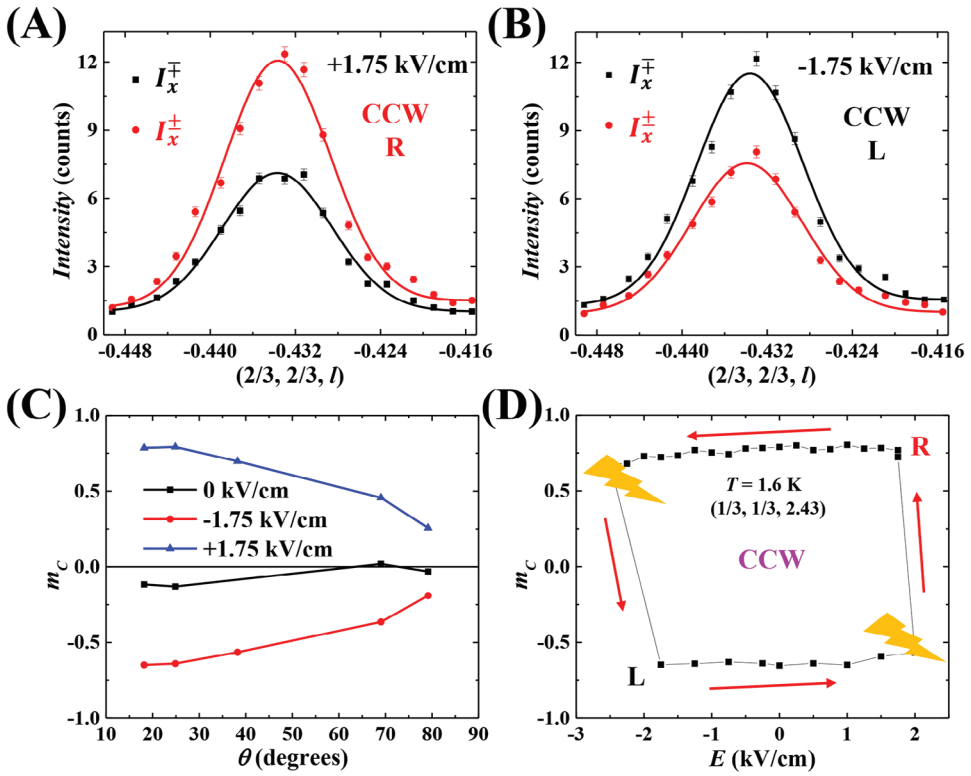

Figure 4. A) Intensities of $I_x^{\pm}$ and $I_x^{\mp}$ measured at (2/3, 2/3, –0.43) with a +1.75 kV cm^{-1} poling field. B) Intensities of $I_x^{\pm}$ and $I_x^{\mp}$ measured at (2/3, 2/3, –0.43) with a –1.75 kV cm^{-1} poling field. C) The angle dependence of the normalized magnetic chirality m_c. The angle θ is the respect to (001) direction. The results were obtained at 1.6 K. D) Electric field dependence of the normalized magnetic chirality m_c. The data were measured at 1.6 K at (1/3, 1/3, 2.43) magnetic peak. The red arrows illustrate the ramping direction of electric fields. All results were measured at 1.6 K. The CCW and CW letters indicate the type of FR domain, and the R and L letters signify the handedness of the magnetic domain.

–1.75 kV cm^{-1}, $I_x^{\mp}$ dominates over $I_x^{\pm}$ at (1/3, 1/3, 0.43). This highlights the switchable magnetic chirality under the electric field for both CCW and CW FR domains. For –1.75 kV cm^{-1}, the estimated m_C is –0.42 for (1/3, 1/3, 0.43).

According to the previous results of the isostructural RFMO, the helical magnetic structure of our RFSO crystals may consist of two types of magnetic chirality: triangular and helical.[1] Nevertheless, the SOS relationships suggest that the FR order and ferroelectric polarization are coupled to the helical chirality. Note that the helical chirality in RFSO arises from the twist along the (001) direction, while the triangular chirality is a result of the in-plane 120° configuration. By analyzing the angle dependence of magnetic chirality between the (001) and (110) directions, we can differentiate the couplings of the FR order and ferroelectric polarization to each of the chirality. Figure 3B shows the $I_x^{\mp}$ and $I_x^{\pm}$ at (1/3, 1/3, 2.43) for the crystal poled with +1.75 kV cm^{-1}. The scattering vector (1/3, 1/3, 2.43) forms an angle of 24.877° with the (001) direction, while the (1/3, 1/3, 0.43) has an angle of 69.023° with the same direction. Notably, the difference between $I_x^{\mp}$ and $I_x^{\pm}$ at (1/3, 1/3, 2.43) peak significantly exceeds that of the (1/3, 1/3, 0.43) peak. The estimated m_C is +0.92 for (1/3, 1/3, 2.43), a value noticeably larger than that of the (1/3, 1/3, 0.43) peak. Figure 3C shows the $I_x^{\mp}$ and $I_x^{\pm}$ for (1/3, 1/3, 2.43) when the crystal is poled by –1.75 kV cm^{-1}. Similar to the (1/3, 1/3, 0.43) peak, the negative electric field inverts the handedness of the magnetic chirality. The estimated m_C is –0.64, again magnitude larger than that of the (1/3, 1/3, 0.43) peak. When the crystal remains unpoled (0 kV cm^{-1}) as shown in Figure 3D, the $I_x^{\mp}$ and $I_x^{\pm}$ showcase nearly identical intensities, indicating the roughly equal distribution of left-and right-handed magnetic domains. For the minor CW FR domain, as shown in Figure 3E,F, the handedness of the magnetic chirality at (1/3, 1/3, 2.56) aligns with that of the (1/3, 1/3, –0.43) peak, albeit with a considerably elevated m_C. The m_C values are –0.81 and +0.63 for +1.75 and –1.75 kV cm^{-1}, respectively.

Figure 4A,B show the $I_x^{\mp}$ and $I_x^{\pm}$ for (2/3, 2/3, –0.43) under various poling electric fields. Note that (2/3, 2/3, –0.43) can be represented as (1, 1, 0) – (1/3, 1/3, 0.43), signifying its origin from the dominant CCW FR domain. However, when compared to (1/3, 1/3, 0.43) and (1/3, 1/3, 2.43), the (2/3, 2/3, –0.43) is proximal to the (110) direction given its minimal angle of 10.841° with it. Intriguingly, for both ±1.75 kV cm^{-1}, the difference between $I_x^{\mp}$ and $I_x^{\pm}$ is notably reduced compared to that of the (1/3, 1/3, 0.43) and (1/3, 1/3, 2.43) peaks. The estimated m_C are +0.26 and –0.19 for +1.75 and –1.75 kV cm^{-1}, respectively. If the crystal is unpoled (see Figure S4B, Supporting Information), the $I_x^{\mp}$ is almost identical with $I_x^{\pm}$. We also measured the $I_x^{\mp}$ and $I_x^{\pm}$ at magnetic peaks of (1/3, 1/3, 1.43) and (1/3, 1/3, 3.43). The m_C values for all magnetic peaks are summarized in Figure 4C, plotted against the angle θ relative to the (001) direction. For both +1.75 and –1.75 kV cm^{-1}, the m_C value decreases with increasing θ. This trend aligns with the SOS findings, reinforcing the coupling of FR order

© 2024 The Author(s). Advanced Science published by Wiley-VCH GmbH

and ferroelectric polarization with helical rather than triangular chirality.

To assess the ferroelectric memory effect on magnetic chirality, we measured the m_C at (1/3, 1/3, 2.43) peak at 1.6 K as a function of an electric field. Before the measurement, the crystal was poled with +1.75 kV cm^{-1}. Figure 4D reveals that the m_C remains constant even as the electric field transitions from a non-zero value to zero. It retains both its sign and value, even when subjected to negative electric fields, underscoring the ferroelectric memory effect. The m_C is expected to change its sign when the electric field surpasses the coercive field of ferroelectricity. Yet, the coercive field of RFSO might be considerably high, and the electric current leakage occurs at –2.5 kV cm^{-1} before reaching the coercive field. This electric current leakage produces heat, raising the crystal's temperature to ≈10 K. Post-cooling to 1.6 K, with the crystal effectively conditioned under –1.75 kV cm^{-1}, the m_C reversed, settling a value of –0.64. Subsequent ramping from –1.75 to +2.0 kV cm^{-1} caused another electric current leakage at +2.0 kV cm^{-1}, altering m_C via the thermal cycle.

3. Conclusion

The research has successfully demonstrated a cost-effective method for growing homo-FR helimagnetic RFSO crystals by lowering the crystal growth temperature below the T_{FR} using the high-pressure hydrothermal method. Polarized neutron diffraction studies have revealed that ≈86% of the RFSO crystal consists of a single FR domain. This growth technique provides valuable insights that can be applied to the production of other homo-FR materials. Furthermore, the X-ray diffraction analysis has confirmed that RFSO exhibits an exceptionally high T_{FR} of ≈573 K, which significantly exceeds the T_{FR} values of RFMO and CMO. This remarkable T_{FR} in RFSO is attributed to the presence of SO_4 ions that promote rotational distortions. The findings suggest that the search for new FR materials with high T_{FR} should consider sulfates as promising candidates.

Additionally, our investigation reveals that RFSO crystals exhibit chiral helimagnetic order, and their magnetic chirality can be manipulated by altering the direction of ferroelectric polarization through an external electric field. Recent theoretical calculations suggest that these helimagnets can generate nonreciprocal spin waves, which can either arise from the Dzyaloshinskii–Moriya interaction or when external magnetic fields are present.[35,17] The growing interest in nonreciprocal spin waves in materials is due to their potential for constructing logic devices like spin-wave diodes.[16,36,37] The homo-FR helimagnetic RFSO crystals offer an ideal platform for investigating nonreciprocal spin waves in future research. Notably, the controllability of the magnetic chirality of RFSO via an external electric field opens up exciting possibilities. This controllability makes homo-FR RFSO crystals a promising candidate for harnessing nonreciprocal spin waves through electric fields and facilitating the development of future device configurations, such as electric-field-tunable spin-wave diodes. This study not only presents a reliable method for growing homo-FR crystals but also underscores the potential for synthesizing new homo-FR materials with unique properties and applications.

4. Experimental Section

Single crystals of RFSO were synthesized using a hydrothermal method in a 50-mL Teflon-lined autoclave. A sulfuric acid solution containing Rb_2SO_4 and $Fe_2(SO_4)_3$ in a 1:1 molar ratio was subjected to hydrothermal treatment at 483 K for 72 h. After the growth process, hexagonal crystals with a ruby color were extracted from the solution. Single crystal X-ray diffraction was conducted at beamline 15-ID-D at the Advanced Photon Source, Argonne National Laboratory, with a 0.41328 Å wavelength. Modeling of multiply redundant full-sphere single crystal diffraction data sets was performed using Olex2, including absorption corrections and anomalous scattering corrections. Powder X-ray diffraction data were collected at Beamline 28-ID-1 (PDF) at the National Synchrotron Light Source (NSLS2), Brookhaven National Laboratory, using a 0.1665 Å wavelength. Measurements were conducted on a powder sample (crushed single crystals) in a quartz capillary. RA-SHG measurements were performed using an ultrafast light source with 800 nm wavelength, 40 fs pulse duration, and 200 kHz repetition rate. An achromatic lens with a beam size of 25 µm was employed, and the intensity of the reflected SHG was measured with a photomultiplier tube. Bulk magnetization was measured using a Vibrating Sample Magnetometer. The dielectric constant was determined at 1 kHz using an LCR meter, and ferroelectric polarization was measured by the pyro-current method with an electrometer. Unpolarized neutron diffraction was performed at the BT4 triple-axis spectrometer (2.36 Å wavelength) at the NIST Center for Neutron Research. Polarized neutron diffraction was carried out at HB1 triple-axis spectrometer (2.46 Å wavelength) at the High Flux Isotope Reactor, Oak Ridge National Laboratory, using Heusler alloy monochromators and analyzers.

DFT calculations were conducted using the Vienna ab initio Simulation Package, employing projector-augmented wave pseudo-potentials.[38–40] Supercells (2 × 2 × 2) of the original 12 atom unit cells were created. The geometries of these crystal structures were fully optimized (lattice parameters and atomic positions) using a 700 eV plane wave cutoff, 3 × 3 × 2 Monkhorst–Pack *k*-point mesh, energy convergence of 10^{-6} eV, force convergence of 10^{-3} eV Å^{-1}.[41] The Perdew–Burke–Ernzerhof functional revised for solids (PBEsol) was utilized[42]; the lattice parameters of RFSO optimized using this functional (a = 4.8633 Å, c = 8.2636 Å) were in excellent agreement with the experimental results (Table S1, Supporting Information). A Hubbard U correction of U = 4.0 eV was applied to the Fe d-states, in accordance with the analysis done in previous works.[43,44] To obtain the energy as a function of the MO_4 rotation angle, intermediate structures were created and the energy was computed self-consistently with a convergence tolerance of 10^{-8} eV.

Supporting Information

Supporting Information is available from the Wiley Online Library or from the author.

Acknowledgements

J.Y. acknowledges support by DOE under Grant No. DOE: DE-SC0021188. T.A.T. acknowledges support from NSF DMR-2313456. L.Z. acknowledges support from the AFOSR YIP grant no. FA9550-21-1-0065, NSF CAREER grant no. DMR-174774 and Alfred P. Sloan Foundation. S.W.C. was supported by the DOE under Grant No. DOE: DE-FG02-07ER46382. This research used resources at the High Flux Isotope Reactor, a DOE Office of Science User Facility operated by the Oak Ridge National Laboratory. DFT calculations were performed on the Lochness cluster at the NJIT and on the Carbon cluster at the Center for Nanoscale Materials, Argonne National Laboratory. Work performed at the Center for Nanoscale Materials, a U.S. Department of Energy Office of Science User Facility, was supported by the U.S. DOE, Office of Basic Energy Sciences, under Contract No. DE-AC02-06CH11357. The following Carbon allocation numbers were used for this work: CNM 72794, CNM 75950 and CNM 82184. Single crystal X-ray diffraction measurements were conducted at NSF's ChemMatCARS, Sector 15 at the Advanced Photon Source, Argonne National

© 2024 The Author(s). Advanced Science published by Wiley-VCH GmbH

Laboratory is supported by the Divisions of Chemistry (CHE) and Materials Research (DMR), National Science Foundation, under grant number NSF/CHE- 1834750. High-temperature powder X-ray diffraction measurements were conducted at beamline 28-ID-1 of the National Synchrotron Light Source II, the National Synchrotron Light Source II, a U.S. Department of Energy (DOE) Office of Science User Facility operated for the DOE Office of Science by Brookhaven National Laboratory under Contract No. DE-SC0012704. Any mention of commercial products is for information only; it does not imply recommendation or endorsement by NIST.

Conflict of Interest

The authors declare no conflict of interest.

Data Availability Statement

The data that support the findings of this study are available from the corresponding author upon reasonable request.

Keywords

ferro-rotation, helimagnet, magnetic chirality, multiferroic, neutron diffraction, single crystal growth

Received: February 26, 2024
Revised: April 29, 2024
Published online: July 3, 2024

[1] A. J. Hearmon, F. Fabrizi, L. C. Chapon, R. D. Johnson, D. Prabhakaran, S. V. Streltsov, P. J. Brown, P. G. Radaelli, *Phys. Rev. Lett.* **2012**, *108*, 237201.
[2] R. D. Johnson, L. C. Chapon, D. D. Khalyavin, P. Manuel, P. G. Radaelli, C. Martin, *Phys. Rev. Lett.* **2012**, *108*, 067 201.
[3] J. Hlinka, J. Privratska, P. Ondrejkovic, V. Janovec, *Phys. Rev. Lett.* **2016**, *116*, 177602.
[4] T. Hayashida, Y. Uemura, K. Kimura, S. Matsuoka, D. Morikawa, S. Hirose, K. Tsuda, T. Hasegawa, T. Kimura, *Nat. Commun.* **2020**, *11*, 4582.
[5] W. Jin, E. Drueke, S. Li, A. Admasu, R. Owen, M. Day, K. Sun, S. W. Cheong, L. Zhao, *Nat. Phys.* **2020**, *16*, 42.
[6] T. Hayashida, Y. Uemura, K. Kimura, S. Matsuoka, M. Hagihala, S. Hirose, H. Morioka, T. Hasegawa, T. Kimura, *Phys. Rev. Mater.* **2021**, *5*, 124409.
[7] X. Luo, D. Obeysekera, C. Won, S. H. Sung, N. Schnitzer, R. Hovden, S. W. Cheong, J. Yang, K. Sun, L. Zhao, *Phys. Rev. Lett.* **2021**, *127*, 126401.
[8] R. Owen, E. Drueke, C. Albunio, A. Kaczmarek, W. Jin, D. Obeysekera, S. W. Cheong, J. Yang, S. Cundiff, L. Zhao, *Phys. Rev. B* **2021**, *103*, 054104.
[9] X. Guo, R. Owen, A. Kaczmarek, X. Fang, C. De, Y. Ahn, W. Hu, N. Agarwal, S. H. Sung, R. Hovden, S. W. Cheong, L. Zhao, *Phys. Rev. B* **2023**, *107*, L180102.
[10] W. Jin, *Nat. Nanotechnol.* **2023**, *18*, 840.
[11] G. Liu, T. Qiu, K. He, Y. Liu, D. Lin, Z. Ma, Z. Huang, W. Tang, J. Xu, K. Watanabe, T. Taniguchi, L. Gao, J. Wen, J. M. Liu, B. Yan, X. Xi, *Nat. Nanotechnol.* **2023**, *18*, 854.
[12] J. S. White, C. Niedermayer, G. Gasparovic, C. Broholm, J. M. S. Park, A. Y. Shapiro, L. A. Demianets, M. Kenzelmann, *Phys. Rev. B.* **2013**, *88*, 060409.
[13] S. W. Cheong, D. Talbayev, V. Kiryukhin, A. Saxena, *npj Quantum Mater.* **2018**, *3*, 19.
[14] D. I. Khomskii, *J. Magn. Magn. Mater.* **2006**, *306*, 1.
[15] M. Bibes, A. Barthélémy, *Nat. Mater.* **2008**, *7*, 425.
[16] M. Jamali, J. H. Kwon, S. M. Seo, K. J. Lee, H. Yang, *Sci. Rep.* **2013**, *3*, 3160.
[17] F. J. Dos Santos, M. Dos Santos Dias, S. Lounis, *Phys. Rev. B.* **2020**, *102*, 104401.
[18] N. Ogawa, L. Köhler, M. Garst, S. Toyoda, S. Seki, Y. Tokura, *Proc. Natl. Acad. Sci.* **2021**, *118*, 2022927118.
[19] G. Shirane, S. J. Pickart, Y. Ishikawa, *J. Phys. Soc. Jpn.* **1959**, *14*, 1352.
[20] G. Shirane, S. J. Pickart, R. Nathans, Y. Ishikawa, *J. Phys. Chem. Solids.* **1959**, *10*, 35.
[21] D. V. West, Q. Huang, H. W. Zandbergen, T. M. McQueen, R. J. Cava, *J. Solid State Chem.* **2008**, *181*, 2768.
[22] H. Serrano-González, S. T. Bramwell, K. D. M. Harris, B. M. Kariuki, L. Nixon, I. P. Parkin, C. Ritter, *Phys. Rev. B* **1999**, *59*, 14451.
[23] T. Inami, *J. Solid State Chem.* **2007**, *180*, 2075.
[24] H. Serrano-González, S. T. Bramwell, K. D. M. Harris, B. M. Kariuki, L. Nixon, I. P. Parkin, C. Ritterm, *J. Appl. Phys.* **1998**, *83*, 6314.
[25] P. V. Klevtsov, R. F. Klevtsova, *J. Struct. Chem.* **1977**, *18*, 339.
[26] S. A. Klimin, M. N. Popova, B. N. Mavrin, P. H. M. M. van Loosdrecht, L. E. Svistov, A. I. Smirnov, L. A. Prozorova, H. K. von Nidda, Z. Seidov, A. Loidl, A. Y. Shapiro, *Phys. Rev. B.* **2003**, *68*, 174408.
[27] A. S. Wills, *Phys. Rev. B.* **2001**, *63*, 64430.
[28] A. S. Wills, *Phys. B* **2000**, *276*, 680.
[29] E. F. Bertaut, *Acta Crystallogr. A* **1968**, *24*, 217.
[30] E. F. Bertaut, *J. Magn. Magn. Mater.* **1981**, *24*, 267.
[31] S.-W. Cheong, X. Xu, *npj Quantum Mater.* **2022**, *7*, 40.
[32] S. W. Cheong, *npj Quantum Mater.* **2019**, *4*, 53.
[33] S. W. Cheong, F. T. Huang, M. Kim, *Rep. Prog. Phys.* **2022**, *85*, 124501.
[34] S. W. Cheong, S. Lim, K. Du, F. T. Huang, *npj Quantum Mater.* **2021**, *6*, 58.
[35] S. Cheon, H. W. Lee, S. W. Cheong, *Phys. Rev. B* **2018**, *98*, 184405.
[36] D. Seo, S. Hwang, B. Kim, Y. Yang, S. Yoon, B. K. Cho, *Sci. Rep.* **2021**, *11*, 24385.
[37] Q. Wang, A. V. Chumak, P. Pirro, *Nat. Commun.* **2021**, *12*, 2636.
[38] P. Hohenberg, W. Kohn, *Phys. Rev.* **1964**, *136*, B864.
[39] G. Kresse, J. Furthmüller, *Phys. Rev. B.* **1996**, *54*, 11169.
[40] P. E. Blöchl, *Phys. Rev. B* **1994**, *50*, 17953.
[41] H. J. Monkhorst, J. D. Pack, *Phys. Rev. B* **1976**, *13*, 5188.
[42] J. P. Perdew, A. Ruzsinszky, G. I. Csonka, O. A. Vydrov, G. E. Scuseria, L. A. Constantin, X. Zhou, K. Burke, *Phys. Rev. Lett.* **2008**, *100*, 136406.
[43] J. Hubbard, *Proc. Roy. Soc. Lond. A* **1963**, *276*, 238.
[44] K. Cao, R. D. Johnson, F. Giustino, P. G. Radaelli, G. C. Guo, L. He, *Phys. Rev. B* **2014**, *90*, 024402.

© 2024 The Author(s). Advanced Science published by Wiley-VCH GmbH